Methods 207 (2022) 44–56

Contents lists available at ScienceDirect

Methods

journal homepage: www.elsevier.com/locate/ymeth

Guide to studying intrinsically disordered proteins by high-speed atomic force microscopy

Noriyuki Kodera, Toshio Ando *

Nano Life Science Institute (WPI-NanoLSI), Kanazawa University, Kakuma-machi, Kanazawa 920-1192, Japan

ARTICLE INFO

Keywords:
Intrinsically disordered proteins
Dynamic structure
High-speed AFM
Bioimaging

ABSTRACT

Intrinsically disordered proteins (IDPs) are partially or entirely disordered. Their intrinsically disordered regions (IDRs) dynamically explore a wide range of structural space by their highly flexible nature. Due to this distinct feature largely different from structured proteins, conventional structural analyses relying on ensemble averaging is unsuitable for characterizing the dynamic structure of IDPs. Therefore, single-molecule measurement tools have been desired in IDP studies. High-speed atomic force microscopy (HS-AFM) is a unique tool that allows us to directly visualize single biomolecules at 2–3 nm lateral and ~ 0.1 nm vertical spatial resolution, and at sub-100 ms temporal resolution under near physiological conditions, without any chemical labeling. HS-AFM has been successfully used not only to characterize the shape and motion of IDP molecules but also to visualize their function-related dynamics. In this article, after reviewing the principle and current performances of HS-AFM, we describe experimental considerations in the HS-AFM imaging of IDPs and methods to quantify molecular features from captured images. Finally, we outline recent HS-AFM imaging studies of IDPs.

1. Introduction

Many proteins contain intrinsically disordered regions (IDRs) lacking stable secondary and tertiary structure. And yet, they can carry out biological functions. These proteins, called intrinsically disordered proteins (IDPs), are involved in a variety of cellular processes, such as signaling and regulation of transcription, translation and cell cycle [1,2] as well as the formation of liquid droplet-like membrane-less organelles (MLOs) [3,4]. IDRs are highly flexible and dynamic; the amino acid residues in an IDR responsible for intramolecular interactions and target binding are widely distributed in space and time. This highly flexible nature facilitates weak but frequent intramolecular interactions between distantly separated regions within an IDP. The flexibility also facilitates the structural adaptation of an IDP to a binding partner, and hence, enables multiple targets binding and multiple functions [5]. The IDPs' functional and regulatory manners are therefore distinctly different from those of structured proteins. Hence, IDPs can execute unique biological functions unattainable with structured proteins. As such, characterizing the dynamic structure of IDPs is essential for understanding the mechanisms underlying their function and regulation.

However, this characterization is considerably difficult because of lack of experimental methods that can delineate and quantify the dynamic structure of IDPs. In ensemble averaging methods, such as nuclear magnetic resonance (NMR) spectroscopy and small angle X-ray scattering (SAXS), individual conformers and their populations can only be examined by relying on structural and/or ensemble modeling [6–8]. Moreover, NMR can hardly distinguish between fully disordered and loosely folded IDRs, and SAXS can hardly detect short-lived structures. Although the single-molecule Förster resonance energy transfer method can probe the structural heterogeneity and kinetics of IDPs, the structural information is limited to the distance between two intramolecular residues separated by less than 10 nm [9]. Molecular dynamics simulations can derive ensembles of disordered structures at the atomic level [10,11]. However, validating the simulated results is difficult because the corresponding experimental information is limited. Therefore, the lack of experimentally obtainable dynamic structural information due to the absence of appropriate methods has hampered our understanding of

Abbreviations: IDP, Intrinsically dissordered protein; IDR, Intrinsically disordered region; AFM, Atomic force microscopy; HS-AFM, High-speed atomic force microscopy; NMR, Nuclear magnetic resonance; SAXS, Small angle X-ray scattering; FACT, Facilitates chromatin transcription; MLO, Membrane-less organelle; LLPS, Liquid–liquid phase separation; PID, proportional-integral-derivative; MBP, Maltose binding protein; Trx, Thioredoxin; GFP, Green fluorescent protein; GST, Glutathione S-transferase; HMG, high-mobility-group; LCD, low complexity domain.

* Corresponding author.
E-mail address: tando@staff.kanazawa-u.ac.jp (T. Ando).

https://doi.org/10.1016/j.ymeth.2022.08.008
Received 4 May 2022; Accepted 16 August 2022
Available online 30 August 2022

the functional and regulatory mechanisms of IDPs.

In contrast to these methods, high-speed atomic force microscopy (HS-AFM), a recently emerged microscopy technique, can directly visualize the dynamic structure of single molecules at sub-molecular spatial and sub-100 ms temporal resolution, without any labeling [12,13]. In 2008, it was demonstrated for the first time that HS-AFM can directly visualize the thin structure of IDRs in dynamic motion, using a model protein, facilitates chromatin transcription (FACT) protein [14], although the performance of HS-AFM at the time was lower than that of the current version. Since then, HS-AFM has been used to observe IDPs. The filmed images have successfully quantified dynamic structural features of several IDPs [15–20]. In addition, function-related phenomena of IDPs have also been visualized by HS-AFM. For example, the peptidoglycan layer binding domain of MotPS, a stator ring of the sodium-ion driven bacterial flagellar motor, was observed to undergo a structural transition from the unfolded to the folded state when exposed to sodium ions [21]. Moreover, the following phenomena were also observed: the cross-β polymerization of α-synuclein and Sup35 [22,23], the assembly process of translation factors around the ribosomal stalk complex [24] and the formation of the droplet-like autophagy initiation complex by liquid–liquid phase separation (LLPS) [25]. In the following sections, we first overview the principle and performances of HS-AFM, and then describe experimental considerations for HS-AFM imaging of IDPs as well as methods to quantify structural features of IDPs from filmed images. Finally, several HS-AFM studies on IDPs are outlined.

2. Performance of high-speed AFM

2.1. Principle of high-speed AFM

The principle and the system configuration of HS-AFM are basically the same as those of conventional AFM but the instrumental components are optimized for fast imaging. In brief, AFM captures the topographic images of a sample surface by tracing the surface with a tip attached to the free end of a micro cantilever (Fig. 1a). Therefore, AFM cannot observe the interior structure of the sample. Moreover, AFM cannot observe objects floating in solution, and therefore, the target objects generally have to be placed on a substrate surface. For fragile biological samples, the amplitude modulation mode is usually used [26–28], in which the cantilever oscillates in the Z direction at around its resonance frequency. Therefore, the tip makes intermittent contact with the sample surface, which reduces the cantilever oscillation amplitude. The cantilever deflection is monitored by the laser light reflected back from the cantilever, which is guided to a position-sensitive (bi-cell or quadrant) photodiode. The output signals from the photodiode are converted to an amplitude signal. Then, a deferential signal (error signal) between the detected amplitude and a preset amplitude value (i.e., the feedback set point amplitude) is fed into to a proportional-integral-derivative (PID) feedback controller. The output signal from the feedback controller is sent to a Z-piezo driver to move the Z-scanner (and the sample stage) in the Z-direction so that the error signal approaches zero. This series of operations are continuously repeated at different points on the sample surface during lateral (XY) scanning of the sample stage. As a result, the sample surface topography can be reconstructed from the recorded feedback controller output.

To materialize HS-AFM, all the mechanical and electronic components have been optimized for fast scanning in the XYZ directions (especially in the Z-direction) and for the fast response and detection of cantilever oscillation amplitude (Fig. 1b). To perform HS-AFM imaging for fragile biomolecules, the feedback control speed should be high enough so that the tip-disturbance to the sample can be minimized. As characteristic devices in HS-AFM, the following instrumental components and techniques have been developed: small cantilevers with a small spring constant (k_c) and a high resonance frequency (f_c) [12], an optical beam deflection detection system specialized for small cantilevers [12], a high-speed amplitude detector [12], a dynamic PID feedback controller with an automatic gain control capability [29], high-speed scanners [12], and active vibration damping techniques for the scanners [30]. Details of the instrumental development are described elsewhere [31]. For more comprehensive descriptions of the fundamentals, techniques and biological applications of HS-AFM, a book is available [32].

2.2. Temporal resolution of high-speed AFM

As mentioned above, the speed performance of an AFM system is determined by the feedback control speed represented by the feedback bandwidth, f_B. It is defined by the feedback frequency at which π/4 phase delay occurs in tip-tracing of the sample surface topography. The minimum time to acquire an image T_{min}, namely the temporal resolution, depends on the imaging conditions (the number of scan lines, N; the scan range in the X-direction, W), the smallest sample surface corrugation to be observed (σ) and the sample fragility, and given as

$$T_{min} = \frac{\pi NW}{2\sigma\theta_{max}f_B},$$

where θ_{max} is the maximum possible phase delay in tracing the sample

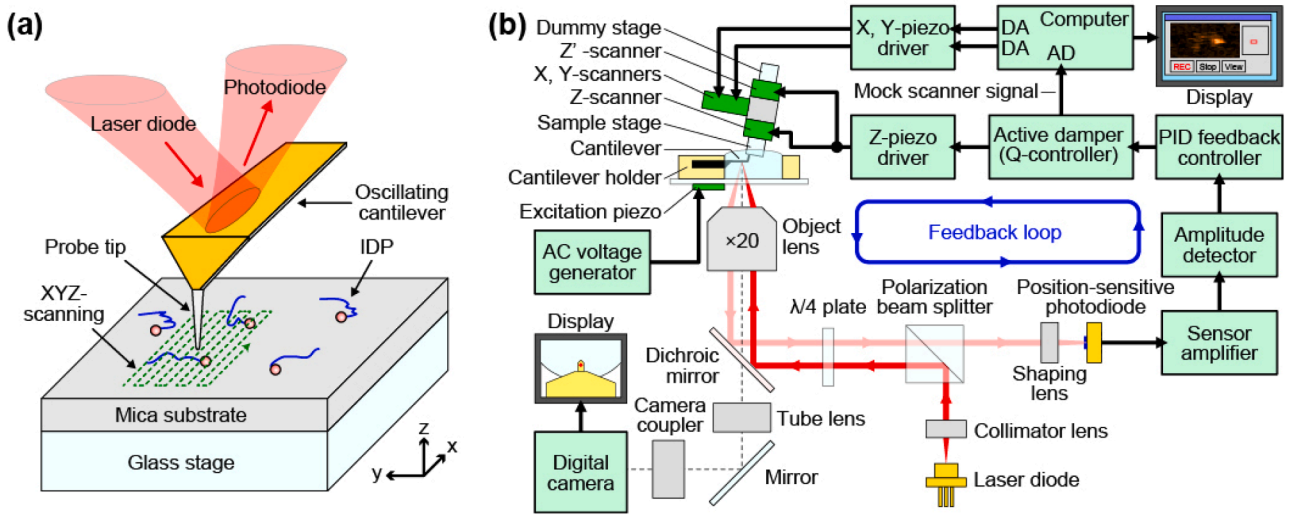

Fig. 1. Principle of AFM and high-speed AFM system. (a) Schematic showing the principle of AFM imaging. (b) Diagram of high-speed AFM system.

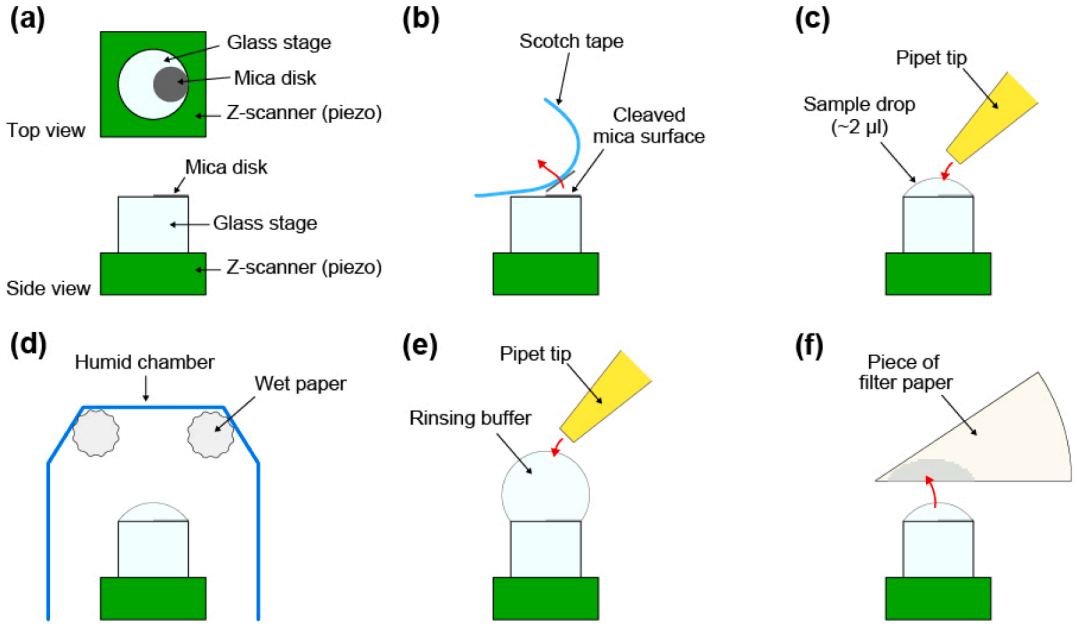

Fig. 2. Procedure of sample deposition on bare mica surface (from a to f).

surface at which the resulting excessive force exerted from the tip does not disturb the biological function of the sample [33]. Using the image acquisition time per frame T ($\geqq T_{min}$), the tip velocity V_{tip} at a given scanning condition is obtained as $V_{tip} = 2NW/T$. f_B is usually affected by a combination of other parameters (i.e., the cantilever free oscillation amplitude, the feedback set point amplitude and the sample height). However, these parameters do not have a large effect on f_B (hence on T_{min}) in the observation of IDPs because the molecular height of IDPs is generally low, comparable to or smaller than the cantilever oscillation amplitude (1–2 nm). The current HS-AFM system has achieved $f_B = 110$ kHz for low height samples. Although θ_{max} depends on the sample fragility, it is typically $\sim \pi/9$ for proteins, according to previous imaging studies on structured proteins [34]. For example, under the conditions of $f_B = 110$ kHz, $W = 80$ nm, $N = 80$, $\theta_{max} = \pi/9$, and $\sigma = 5$ nm, T_{min} becomes ~ 50 ms, corresponding to an imaging rate of ~ 20 frames per second (fps). In addition, as described below, it has been confirmed that some IDPs with $\sigma \approx 2$ nm can be imaged without deteriorating their morphological and dynamic features even under observation conditions where θ_{max} probably exceeds $\pi/9$ [19]. This is largely due to the very low height of IDRs, corresponding to the diameter of a single polypeptide chain.

2.3. Spatial resolution of high-speed AFM

The spatial resolution of HS-AFM in the XY direction is typically 2–3 nm and $\sim$ 1 nm in the best case, which is largely dependent on the cantilever's tip size. Some commercially available cantilevers for HS-AFM have a sharp tip with a radius less than 5 nm (e.g., USC-F1.2-k0.15 or USC-F1.2-k0.6, NanoWorld, Switzerland), but they become blunt after use, due to smearing.

To obtain a sharp tip, we fabricate a tip by spot deposition of electron beam onto the original tip in an atmosphere of gas supplied from sublimate ferrocene crystals in the chamber of a scanning electron microscope [35]. The fabricated tip length is 0.5–1 µm and the tip end radius is about 25 nm. The tip end is sharpened by radio-frequency plasma etching (Tergeo, PIE Scientific, U.S.A.) in argon gas atmosphere (Direct mode, 10 sccm, and 20 W for 1.5 min). After plasma etching, the tip end radius becomes typically $\sim$ 4 nm.

The spatial resolution in the Z-direction is affected by the cantilever's thermal fluctuation and the mechanical vibration noise of the Z-scanner. When observing IDPs with fully unfolded IDRs, the use of small cantilevers with a slightly larger spring constant (e.g., BL-AC7DS-KU2, Olympus, Japan, k_c = 0.2–0.3 N/m or USC-F1.2-k0.6, NanoWorld, Switzerland, $k_c = 0.6$ N/m) compared to that of frequently used ones (e.g., BL-AC10DS-A2, Olympus, k_c = 0.1 N/m or USC-F1.2-k0.15, NanoWorld, $k_c = 0.15$ N/m) reduces the thermal fluctuation noise, making it easier to visualize fully unfolded IDRs. In addition, the Z-scanner should be constructed by using a piezo actuator having a small piezoelectric constant (i.e., small displacement per applied voltage). This is effective in reducing the mechanical noise in the Z-direction because the Z-scanner can be driven with much larger voltage compared to electrical noise. For example, NAC2012 (Noliac, Denmark), PL033.3x (PI, Germany), and PA4JE (Thorlabs, U.S.A.) with dynamic piezoelectric constants below 20 nm/V are useful. By combining such cantilevers and Z-scanners, spatial resolution of $\sim$ 0.1 nm can be routinely achieved in the Z-direction.

Importantly, an AFM image inherently has time differences between pixels. Namely, all pixel data contained in an image are not acquired at the same time but at different times during lateral scanning of the sample stage. Therefore, slow scanning for a fast-moving object results in an image showing a blurred object shape and hence low spatial resolution. Therefore, it is clear that the speed performance of AFM is essential for clearly resolving the flexible shape and motion of IDPs. In the fast imaging study of FACT protein, it was demonstrated that its IDRs are not visible at 1 fps, only slightly seen at 2 fps, can be seen with their end regions being blurred at 5 fps, and can be clearly seen for the entire length at 10 fps. Therefore, an imaging capability of at least 5 fps is required for a HS-AFM system. HS-AFM systems are now commercially available, from RIBM (model SS-NEX), Bruker-JPK (model NanoRacer), and Oxford Instruments (model Cypher VRS1250). Although the speed performances of these products are described in their advertisements, it is highly recommended to check their speed and other performances by demonstration imaging of your own samples.

3. Procedures for High-speed AFM imaging of IDPs

Procedures for HS-AFM imaging of protein molecules have been described in [36]. Here we mainly describe procedures specific to the imaging of IDPs.

3.1. Precautions for high-speed AFM imaging of IDPs

For successful imaging of IDPs with HS-AFM, there are several precautions to keep in mind. Generally, IDPs are more easily degraded by proteases than structured proteins. Sample preparations should prevent protease contamination as much as possible, and protease inhibitors should be added during sample preparation and storage. Similar to the case of observing structured proteins by HS-AFM, IDP samples should be homogeneous as much as possible. Also, the buffer solutions used for sample dilution and observation should be clean enough. This is because AFM cannot distinguish and identify molecular spices from their topographic features, unless the target object has unique structural features. Generally, each sample should be detected as a single band in SDS polyacrylamide gel electrophoresis. When only IDP molecules deposited on a substrate surface are to be observed, the amount of the sample required for a sufficient number of experiments (>20 times) is about 20 μl with a concentration of about 1 μM. For an experiment that requires IDPs be present at a certain concentration in the bulk solution (e.g., in the observations of liquid droplet formation from IDPs), the required amount can be estimated by taking into account the volume of the liquid cell (50–100 μl), the required sample concentration, and the number of experiments.

The substrate surface to be used in HS-AFM observations should be flat enough. Because the mean height of a fully unfolded IDR is ~ 0.5 nm, the substrate surface should be atomically flat. Practically, bare mica is probably the only choice that meets this requirement and an additional requirement, high hydrophilicity. Chemical modification of mica with silane is often useful for observing structured proteins, but it increases the surface roughness. The mica surface is negatively charged. Therefore, most proteins can bind to the surface; even negatively charged proteins can bind to the surface via divalent cations. However, the affinity of fully disordered IDRs for mica is very weak because the local contact area density is very small and distantly separated portions within an IDR behave almost independently of each other due to its high flexibility (its persistence length is ~ 1.18 nm on mica [19]). Therefore, IDPs consisting of only IDRs often diffuse on mica too fast to be visualized even with the current HS-AFM. To slow down the diffusional motion, the solution conditions (i.e., ionic strength, pH, and the sort of ions) have to be optimized. Alternatively, a protein tag (e.g., MBP: maltose binding protein, Trx: thioredoxin, GFP: green florescent protein, or GST: glutathione S-transferase) or a His-tag (when a mica surface treated with nickel ions is used [20]) can be fused to the N- or C-terminus of IDPs. When one end of such an IDP is anchored to the surface, the diffusional motion of the rest portion of the molecule is largely slowed down.

The precautions for HS-AFM imaging of IDPs are summarized as follows:

- The protein sample should be pure as much as possible.
- Avoid contamination of proteases in the sample as much as possible. Protease inhibitors (e.g., PMSF, benzamidine or TPCK) should be added to avoid possible degradation by proteases when preparing and storing the sample.
- Buffer solutions used for dilution and observations should be clean enough. Most of contaminants can be filtered out by a 0.22 μm syringe filter (e.g., PVDF, 0.22 μm pore, 30 mm in diameter, Advangene, USA). For a strict case, a membrane ultrafiltration (e.g., Vivaspin 6, MWCO 3,000, PES, Sartorius, Germany) is useful to remove small contaminants.
- Use mica for visualizing IDPs at the single molecule level.
- Find appropriate buffer conditions by changing the ionic strength, the sort of ions and the pH of observation buffers.
- Use protein tags (e.g., MBP, Trx, GFP, or GST) or His-tag with an affinity for a nickel ions-treated mica surface, when the IDPs are not well anchored and thus move too fast on the mica surface.

3.2. Dilution of IDP samples

All buffer solutions should contain protease inhibitors (e.g., 1 mM PMSF, 0.5 mM benzamidine, or 20 μg/ml TPCK) and be cooled on ice before use. The sample tube to be used for diluted sample storage should be a low protein binding type (e.g., 72.704.600, Sarstedt, Germany), although this remedy does not completely prevent sample loss. The sample diluted to a few nM should be placed on ice and used up within 15 min to avoid sample loss and possible proteolysis. The dilution of an IDP sample is performed as follows:

1. Dilute a stock IDP solution (usually in the order of ~ 10 μM) to 100–200 nM with an appropriate buffer solution.
2. Divide the diluted sample into small aliquots (10–20 μl) using a low protein binding tube. Then, quickly freeze the aliquots using liquid nitrogen and store them in a deep freezer at –80 °C.
3. Just before AFM experiments, thaw an aliquot of the frozen sample and place it on ice. The thawed aliquot should be used up in a day.
4. Dilute the thawed sample to 1–5 nM with an appropriate buffer solution using a low protein binding tube. Then, place the tube on ice. This step should be done between the steps 2 and 4 described in procedure 3.3.

3.3. Deposition of IDP sample on mica surface

The deposition of an IDP sample on bare mica should be done immediately after sample dilution to 1–5 nM. Therefore, the step 4 of procedure 3.2 should be done between the steps 2 and 4 of the procedure described below. It is very important to avoid drying of the deposited sample solution. Otherwise, the sample would be denatured and impurities would appear in AFM images. If experimental results are not reproducible, it is most likely that procedures to be carried out after sample deposition (the steps 5 and 6 described below) have not been performed appropriately. Note that the buffer solution used for sample dilution can be different from an observation buffer. In general, the dilution buffer should have a property of facilitating monodispersion of the sample. For the observation buffer, we may not need to consider this property very strictly because molecules placed on mica have less chance of encountering each other. The sample deposition on bare mica is performed in the following steps (Fig. 2):

1. Glue a mica disk onto the sample stage using an epoxy adhesive. Then, wait for more than 3 h for drying.
2. Glue the sample stage onto the Z-scanner using nail enamel diluted to ~ 30 % with acetone, and leave it for 5–10 min.
3. Dilute the sample to a few nM (follow the step 4 of procedure 3.2).
4. Press a Scotch tape onto the mica disk surface and then smoothly remove the tape from the mica (Fig. 2b). The top layer of the mica is removed with the tape, which can be checked by inspecting the surface of the removed tape.
5. Deposit a drop (2 μl) of the diluted sample solution (1–5 nM) on the freshly cleaved mica disk surface (Fig. 2c). Then, cover the sample stage with a humid hood and wait for 1–3 min (Fig. 2d).
6. To remove unattached molecules, rinse the mica surface three times using an observation buffer solution (20 μl × 3) and a piece of filter paper (Fig. 2e and f).

3.4. High-speed AFM imaging

To quantitatively characterize dynamic structural features of an IDP by HS-AFM imaging, at least ten and ideally more than twenty molecules should be imaged under each experimental condition. This can reinforce that observed dynamic structural features are common to identical molecules. In addition, it is highly recommended to capture ~ 1,000 images (1–2 min) of each molecule at 10–20 fps, although the required number of images depends on how widely and fast the molecules sample

different conformations. When a higher imaging rate is necessary to record highly mobile IDRs, the imaging rate can be increased by narrowing the imaging area; a small scan size in the X-direction (W) and a reduced number of scan lines (N). Although higher imaging rates could be used even for a wide imaging area, the resulting insufficient feedback control (and hence too excessive tip–sample interactions) would alter the dynamic structural features of the IDP under study or fillip the molecules. In the current HS-AFM system, V_{tip} can go up to 400 μm/s without altering the dynamic structural features of IDPs with low heights (<~3 nm), although very recent technical developments now enable a ~ 4-time higher scan velocity [37–39].

HS-AFM imaging of IDPs is performed as follows:

1. Set a cantilever chip to the cantilever holder equipped with the liquid cell.
2. Set the cantilever holder to the HS-AFM apparatus. Gently wash the liquid cell 2–3 times using an observation buffer (50–100 μl) to remove dirt, while sucking the solution using a gel-loading tip or an injection needle connected to an aspirator (e.g., a baby nasal aspirator or a peristatic pump).
3. Fill the liquid cell with an observation buffer (50–100 μl). The volume of the observation buffer to be loaded should always be adjusted at the predefined volume. When the volume exceeds the predefined volume, the excessive solution will contact the piezoactuator used in the Z-scanner, resulting in its short and hence fatal damage upon high voltage application to the piezo.
4. Adjust the position of the incident laser beam from the optical beam deflection (OBD) detector so that it is focused onto the cantilever's free end region. This adjustment can be done by looking at video images captured by an optical system equipped with the HS-AFM apparatus.
5. When the liquid cell is not a closed type, place wet paper towels (e.g., Kim towels) around the cantilever holder to suppress evaporation of the observation buffer.
6. Deposit the sample on the mica surface (follow procedure 3.3).
7. Mount the scanner on the HS-AFM setup so that the sample stage is partly immersed in the buffer solution placed around the cantilever.
8. Readjust the cantilever position and adjust the sample stage position so that the sample stage is placed over or under the cantilever depending on the HS-AFM apparatus to be used.
9. Find the cantilever resonant frequency by measuring the power spectrum of cantilever's thermal deflection.
10. Excite the cantilever at (near) the found resonant frequency by applying AC voltage to an excitation piezoactuator attached to the cantilever holder. Then, adjust the excitation power so that the free oscillation amplitude A_0 becomes 1–2 nm.
11. Set the feedback set point amplitude A_{sp} at ~ 0.8 × A_0 and run the PID feedback controller.
12. Start a coarse tip–sample approach (~1 μm/s) by driving a stepper motor attached to the scanner. This approach is carried out automatically while the signals of cantilever oscillation amplitude and PID output are monitored.
13. When the cantilever gets close to the surface, stop the tip–sample approach and readjust A_0 at 1–2 nm. The closeness in distance can be judged by an optical image appearance of the mica surface and an increase in A_0.
14. Adjust the feedback setpoint amplitude A_{sp} at 0.9–0.95 × A_0 and start a fine tip–sample approach (~ 0.2 μm/s).
15. Once the cantilever tip makes contact with the sample, start imaging under a relatively mild observation condition (e.g.,

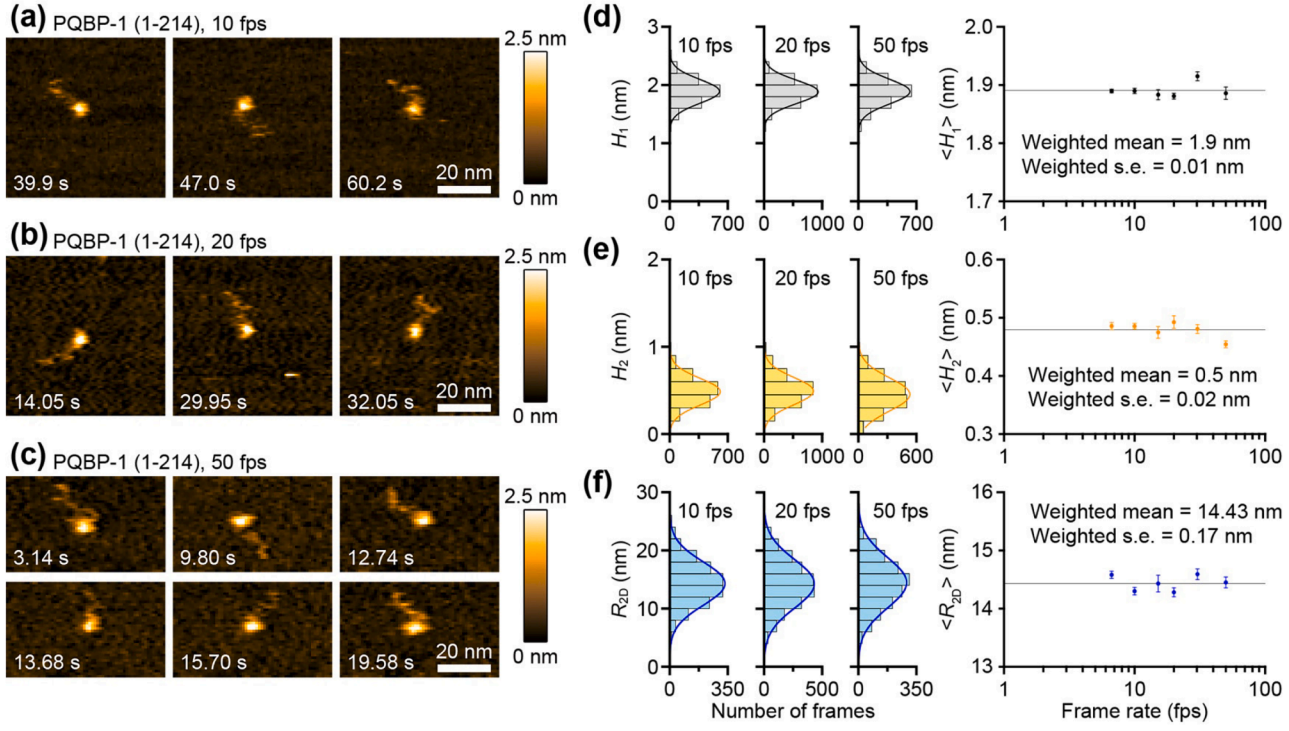

Fig. 3. Molecular features of PQBP-1 (1–214) observed at different imaging rates. (a-c) Clips of successive HS-AFM images of PQBP-1 (1–214) captured at 10 (a), 20 (b) and 50 (c) fps, with 80 × 80 pixels (a, b) and 60 × 36 pixels (c). (d–f) The three graphs in each column of the left three are the histograms for the N-terminal globule height H_1 (d), the IDR end height H_2 (e) and R_{2D} (f) measured from HS-AFM images captured at 10, 20, and 50 fps (from left to rirght). The most probable fitting curves are drawn with the solid lines. The right graphs of (d-f) show $\langle H_1 \rangle$, $\langle H_2 \rangle$ and $\langle R_{2D} \rangle$ at various imaging rates. Each plot corresponds to mean values ± s.e.m. measured at each frame rate. At each condition, more than 1300 frames were analyzed using more than three imaged molecules. The horizontal lines indicate the weighted mean values. The values of $\langle R_{2D} \rangle$, $\langle H_1 \rangle$ and $\langle H_2 \rangle$ are nearly constant, irrespective of the imaging rate, indicating no notable impact of the tip-sample contact on the structure of this protein.

scanning area, 80 × 80 nm^2; the number of pixels, 80 × 80; frame rate, 5 fps; V_{tip}, 160 μm/s).
16. Adjust the feedback control parameters (main I-gain and supportive P-gain) so that clear images appear.
17. Start imaging at 10–20 fps. If necessary, change the observation area by applying DC voltage to the XY-scanner.
18. Collect image data for at least ten molecules (ideally more than twenty molecules) by changing the scanning area.

When molecules moved on the mica surface too fast to be resolved clearly, the observation buffer was probably not appropriate. While changing the ionic strength, the sort of ions and the pH of the solution, repeat the experiments. In this situation, new sample deposition is unnecessary unless the molecules are aggregated under the previous experimental conditions. When the molecules still move too fast on the surface, use an IDP construct fused to a structured protein (e.g., MBP, Trx, GFP, or GST), or a His-tagged sample. When the cantilever tip was not sharp enough to clearly resolve molecular features, just replace the cantilever with a new one, without changing the deposited sample. If necessary, capture images at higher rates up to ~ 50 fps to demonstrate that observed structural features of the molecules are not affected by the tip–sample contact (Fig. 3).

4. AFM image analysis

4.1. Characterization of topographic features of IDPs

Once sufficient image data are collected, the next step is characterizing dynamic structural features of the imaged IDP molecules through image analysis. The first step to this end is to make a list of image frames that seem to contain meaningful data. One of the characteristics of AFM images is that the width of molecular images is strongly affected by the AFM tip size. Therefore, comparing the widths and volumes of molecular images captured for a given sample with different tips is not meaningful. In addition, the quantification of the counter length of an IDR should be done while keeping in mind that its measurement depends on the resolution affected by the tip size. In contrast, the two dimensional end-to-end distance of an IDR (R_{2D}) and the height values (H) at different molecular portions can be reliably quantified.

From the captured HS-AFM images of an IDP, the four dimensional coordinates (x, y, z, t) can be obtained for the following positions of the molecules: the highest positions of globular domains, and various positions of IDRs including the end positions. Note that different positions along a moving IDR cannot be specified accurately, except for its end positions. From the positional coordinates, the time-series data of heights and R_{2D} are acquired. We have carried out image analyses using a laboratory built software that is open to public, including its source code [40]. The procedure is as follows.

1. Make a list of imaged frames that seem to contain meaningful data.
2. Remove spike noise from original images (Fig. 4a) by applying a low pass filter (LPF) (Fig. 4b).
3. Apply a flattening filter so that the substrate surface appears horizontal (Fig. 4c).
4. Apply a line-by-line offset adjustment filter so that the substrate surface height appears constant (Fig. 4d).
5. Obtain the three dimensional coordinates (x_i, y_i, z_i) of the highest positions (P_1) of globular domains, the height of an IDR, and the free end position of an IDR (P_2). This quantification can be done semi-automatically by selecting a region of interest (ROI) (Fig. 4e–g). Also obtain the average height of the mica surface (H_{ave}). Calculate the relative heights H_1 at P_1 and H_2 at P_2 measured from the mica surface as $H_1 = z_1 - H_{ave}$ and $H_2 = z_2 - H_{ave}$. The direct distance D between P_1 and P_2 is calculated, followed by a calculation of R_{2D} value as $R_{2D} = D - H_1/2 - H_2/2$. When an IDR is interspaced between two globular domains, the R_{2D} value can be calculated in a similar way; P_2 is now the highest position of the second globular domain.
6. Obtain the time-series data of H_1, H_2, and R_{2D}.
7. Make graphs (e.g., histograms and time courses of H_1, H_2, and R_{2D}).

In some cases, the height histogram of a globular region is best fitted by a double Gaussian distribution, indicating that the globule has undergone structural transitions. Likewise, when the R_{2D} histogram is best fitted by a double Gaussian distribution, the IDR has undergone structural transitions between partially folded and fully disordered states. The fully disordered state of an IDR can be confirmed by its mean IDR height of ~ 0.5 nm. Therefore, an IDR with a mean height larger than ~ 0.6 nm can be judged to be partially structured. From the double Gaussian distributions of height and R_{2D}, the order propensity of the analyzed regions (K_e) can be estimated by the area ratio of the corresponding double Gaussian components. For more information extractable from HS-AFM images of an IDP, go to procedures 4.2 and 4.3.

4.2. Length rule for fully disordered IDR

From our HS-AFM observations of various IDP constructs placed on mica, we obtained corroborative evidence that the mean R_{2D} values of IDRs, $\langle R_{2D} \rangle$, in the fully disordered state follow the power law, $\langle R_{2D} \rangle = (1.16 \pm 0.057 \text{ nm}) \times N_{aa}^{0.52 \pm 0.009}$, where N_{aa} is the number of amino acids contained in the fully disordered IDRs [19]. Using this power law, the value of N_{aa} can be precisely estimated nearly at the residue level, even when structural information of the IDP under study has not been much available previously. The usefulness of this estimation was demonstrated in the quantitative delineation of dynamic structure of the yeast Cdk1 kinase inhibitor (Sic1) and the N-terminal domain of measles virus (MeV) phosphoprotein (PNT) (Fig. 5) [19].

In the HS-AFM study of Sic1, a construct fused to GFP at the C-terminus of Sic1 was used. The GFP acts as an anchor to the mica surface. Before this HS-AFM study, nothing has been known about the structure and dynamic features of Sic1, other than the qualitative information that Sic1 is disordered over its entire length but has a propensity to adopt a collapsed chain-like form. The histogram of R_{2D} of the IDR between the N-terminal globule and the C-terminal GFP was best fitted to a double Gaussian distribution with peaks at 12.2 ± 0.66 and 20.5 ± 2.14 nm (Fig. 5a). The IDR is fully disordered in both shorter and longer states, as judged from its mean height of ~ 0.5 nm in both metastable states. From the power law, N_{aa} contained in the IDR was estimated to be 95 and 259 for its shorter and longer states, respectively. The height histogram of the N-terminal small globule undergoing transitions was best fitted to a double Gaussian distribution with peaks at 0.9 ± 0.05 nm and 1.3 ± 0.28 nm (Fig. 5b). Therefore, the folding and unfolding transitions in the N-terminal globule result in the length change of the fully unfolded IDR. In fact, the order propensity of the N-terminal globule estimated from the height distribution ($K_e = 1.6$) was nearly identical to that estimated from the R_{2D} distribution ($K_e = 1.5$). From the total number of amino acids contained in Sic1 (284) and the N_{aa} values, the number of amino acids contained in the small globule is approximately estimated to be ~ 30 and ~ 190 for its lower and higher states, respectively (Fig. 5e).

PNT is mostly disordered, but the small regions 1–37, 87–93, and 189–198 were shown by NMR to have α-helical propensities, and hence named $\alpha_{1/2}$, α_3 and α_4, respectively [41]. α_3 and α_4 are interspaced by an acidic IDR (124–168). This structure revealed by NMR could not explain the biochemically detected resistance of the N-terminal 27–99 region to proteolysis [42], suggesting the existence of a large-scale structure undetectable by NMR. The HS-AFM imaging of PNT (1–229) –GFP fusion showed an IDR changing its length and an N-terminal small globule having varying size but a constant height of 1.1 nm (Fig. 5g). This constant height is identical to the height of an α-helix, consistent with the presence of $\alpha_{1/2}$ in the N-terminus. The R_{2D} histogram of the entire IDR was best fitted to a double Gaussian distribution with peaks at 8.9 ± 0.33 and 14.3 ± 9.26 nm (Fig. 5f), corresponding to $N_{aa} = 52$ and $N_{aa} =$

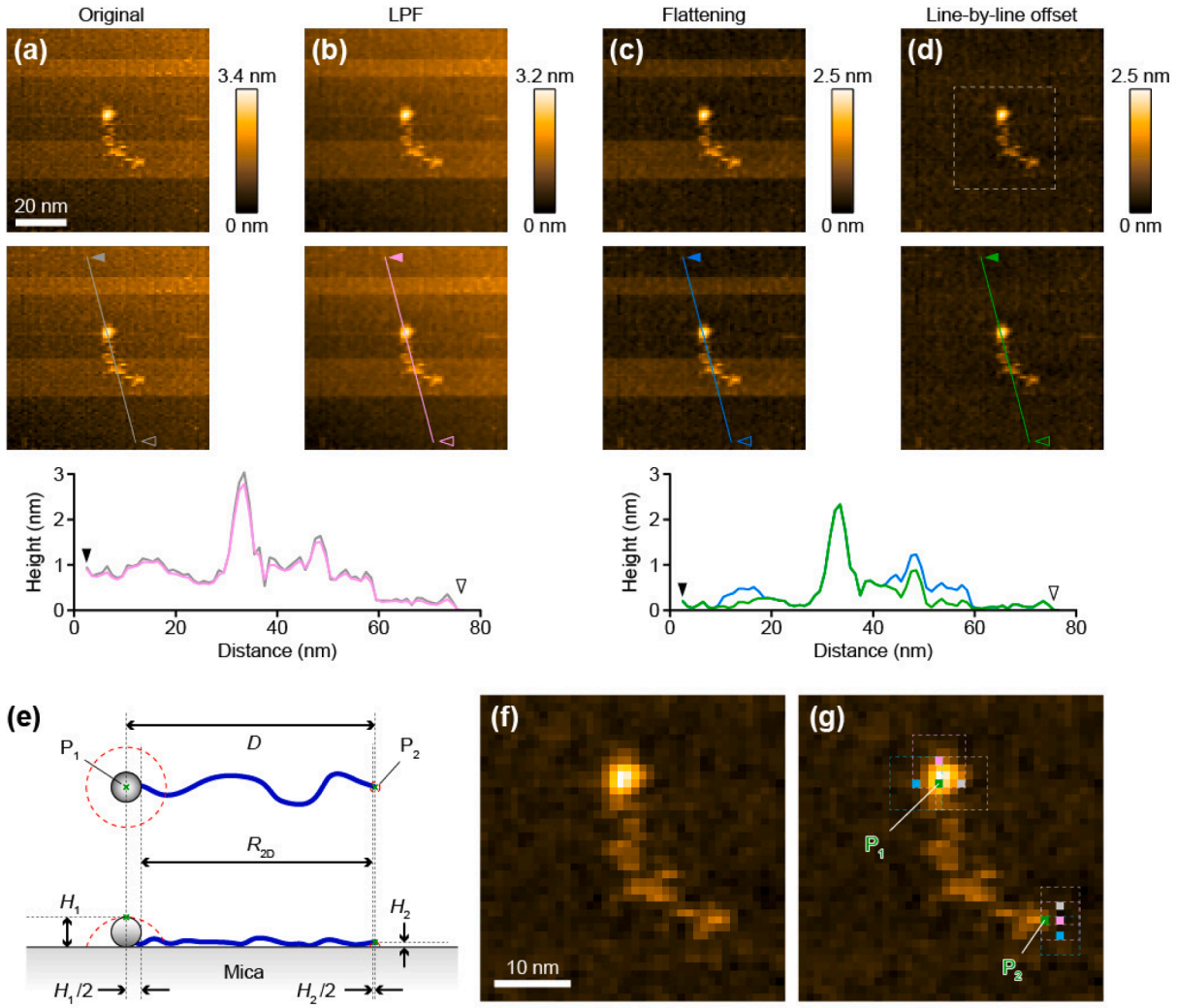

Fig. 4. Procedure of AFM image processing and analysis. (a-d) HS-AFM images of a PQBP-1 molecule for explaining image processing. (a) Original image, (b) after LPF, (c) after flattening filter and (d) after line-by-line offset adjustment. The image was captured with 80 × 80 pixels at 15 fps. The cross-sections along the lines indicated on the second row images are displayed at the bottom to show the effect of each filtering. (e) Schematics showing the observed molecular characteristics of the PQBP-1 molecule (top, top view; bottom, side view): grey spheres, *N*-terminal globular domain; blue thick solid lines, IDRs; dashed red lines, schematic topographies of the globular domain convoluted with the finite size of the tip apex in lateral contact with the globule. (f) Magnified view of the area enclosed by the white dashed line in (d). (g) The same magnified view as (f) explains the semi-automatic selection of two points (P_1 and P_2). The highest point of the globular domain (P_1) and the end region of the IDR (P_2) are searched after the operator clicks the mouse pointer around the globular domain (marked with gray, pink, and light blue) and in a molecule-free region very close to the free end of the IDR (marked with gray, pink, and light blue), respectively. The pixel search program automatically finds P_1 and P_2 by searching over $n \times n$ pixels around the operator-specified pixel positions. The value of n is appropriately chosen. Typically, n is 7 and 5 for the search of P_1 and P_2, respectively. The same points of P_1 and P_2 are selected, irrespective of the different pixels clicked.

129, respectively. From these N_{aa} values, the number of amino acids contained in the small globule is approximately estimated to be ~ 175 and ~ 100 for the shorter and longer IDR states, respectively (Fig. 5i). The number ~ 100 suggests that $\alpha_{1/2}$, α_3 (87–93) and the IDR segment between them (38–86) are contained in the small globule in both the longer and shorter IDR states. Therefore, the region encompassing the *N*-terminus and helix α_3 always forms a compact structure, explaining the resistance to proteolysis of the *N*-terminal segment extending to the 99th residue. The number ~ 175 suggests that the structural transitions between the two states occur mainly by association and dissociation between the *N*-terminal compact structure and the acidic IDR (124–168). The negatively charged residues of this IDR region may contribute to its interaction with the constantly folded small globular domain.

4.3. Structural transition analysis by autocorrelation function

As typically seen in the HS-AFM images of Sic1 and PNT, some IDRs undergo transitions between folded and unfolded conformations. Interestingly, not only IDRs but also other regions that have been thought to be structured exhibit order–disorder transitions. The order propensity and the transiently ordered structures very probably dictate key features in binding of these IDPs to their targets. As indicated above for Sic1 and PNT, the order propensity of an IDR can be estimated by K_e, i.e., the area ratio of the double Gaussian components of height or R_{2D} distribution (Fig. 5a, b and f). Because the time series data of height or R_{2D} can be obtained, the structural transition rates can in principle be estimated from the data. However, the two Gaussian components in double Gaussian fitting often overlap partially. Therefore, we cannot directly estimate the lifetimes of individual conformational states from the time-series data.

We can circumvent this problem by using the autocorrelation function $G(\tau)$ for the time-series data of $R_{2D}(t)$ or $H(t)$. The use of $G(\tau)$ enables the estimation of the order-to-disorder rate constant, K_{OD}, and the disorder-to-order rate constant, k_{DO}, as follows [19]. When the

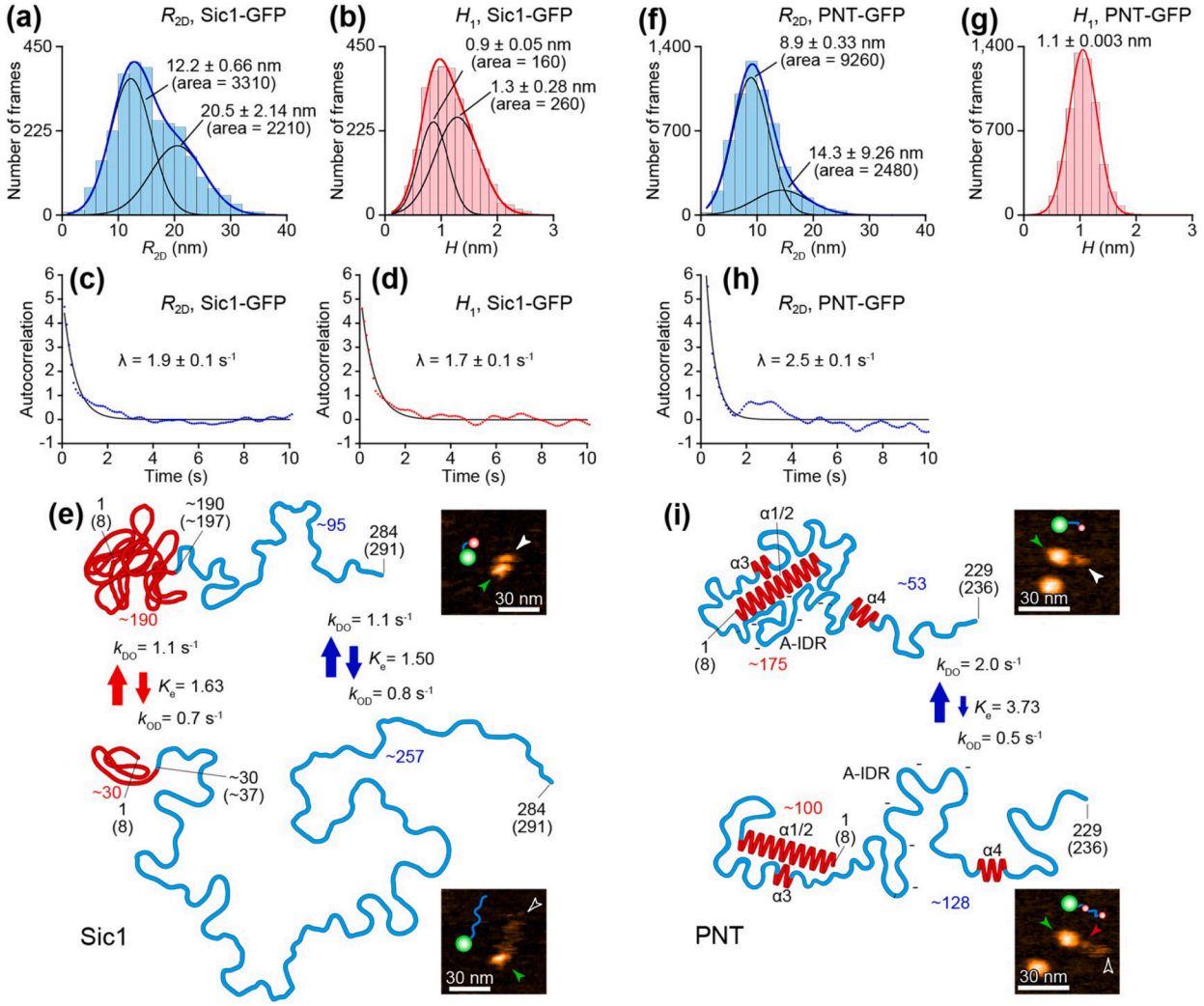

Fig. 5. Dynamic molecular features of Sic1 and PNT revealed by HS-AFM imaging. Extracted dynamic structural information for Sic1-GFP (a-e) and PNT-GFP (f-i). (a, f) R_{2D} distributions in Sic1-GFP (a) and PNT–GFP (f). (b, g) Height distributions of *N*-terminal globules in Sic1-GFP (b) and PNT-GFP (g). (c, d, h) Autocorrelation functions of $R_{2D}(t)$ for IDRs contained in Sic1-GFP (c) and PNT–GFP (h), and an autocorrelation function of H_1(t) data for the *N*-terminal collapsed structure in Sic1-GFP (d). (e, i) Schematics showing structural and dynamic features of Sic1 (e) and PNT (i) revealed by HS-AFM. Insets show typical HS-AFM images together with their sketches: green circles represent the C-terminal GFP moieties, while the red circles represent globules undergoing transitions between folded and unfolded states. In the HS-AFM images, the green arrowheads point to the C-terminal GFP, whereas the closed and open white arrowheads point to the *N*-terminal regions in the folded and unfolded states, respectively. The top and bottom panels correspond to the more- and less-ordered states, respectively. The numbers in red and blue represent the number of amino acids contained in the respective small globules and fully disordered IDRs, respectively. The red and blue arrows show transient changes in $< H_1 >$ (red) and $< R_{2D} >$ (blue).

structural transition of an IDP follows a two-state transition model, the decay rate λ of G(τ) is expressed as $\lambda = k_{OD} + k_{DO}$, while the order propensity K_e is expressed as $K_e = k_{DO}/k_{OD}$. Therefore, the individual rate constants can be expressed as $k_{OD} = \lambda/(1 + K_e)$ and $k_{DO} = \lambda K_e/(1 + K_e)$. The structural transition rates for Sic1 and PNT were estimated in this way (Fig. 5c,d and h). In Sic1, the $G(\tau)$ for $H(t)$ of the *N*-terminal globule and the $G(\tau)$ for $R_{2D}(t)$ were nearly identical, indicating that the increased/decreased height of the *N*-terminal globule is coupled with the folding/unfolding of the IDR. When an IDR is always disordered, the $G(\tau)$ for $R_{2D}(t)$ is zero except for $\tau = 0$, although $R_{2D}(t)$ widely varies due to the flexible nature of the IDR. In fact, this necessary consequence was verified by the $G(\tau)$ for $R_{2D}(t)$ measured for the constantly disordered IDR in PQBP-1 [19].

Autocorrelation function analysis is carried out as follow:

1. Capture HS-AFM movies of IDP molecules successively. The structural transitions occurring on a single molecule should be captured repeatedly in a single movie to produce a time-series datum analyzable by $G(\tau)$. To produce a $G(\tau)$ with a high S/N ratio, the images should be captured at >10 fps, as long as possible (longer than 1 min for each molecule).
2. Analyze the images to obtain the time series data of $R_{2D}(t)$ and/or $H(t)$.
3. When the histogram of all data set of $R_{2D}(t)$ or $H(t)$ is best fitted by a double Gaussian distribution, calculate K_e from the areas of individual Gaussian components. The data fitting should be statistically verified using *F*-test.
4. Calculate an autocorrelation function $G(\tau)$ for each time-series datum of $R_{2D}(t)$ or $H(t)$, and then take an average of $G(\tau)$s.
5. Calculate the decay rate λ of $G(\tau)$ by fitting the averaged $G(\tau)$ to a single exponential function.
6. Calculate k_{OD} and k_{DO} using K_e and λ.

While the estimated transition rates reflect the dynamic structural properties of the molecules under study, their values should be treated with caution. This is because the interactions between the molecules and

mica slow down the molecular motion, which may reduce the transition rates. However, there is currently no way to compare the structural transition rates measured on mica to those in solution because of the paucity of techniques capable of measuring the rates in solution.

5. Imaging studies of IDPs by high-speed AFM

5.1. Morphological changes of IDR induced by post-translational modification

HS-AFM can be used to investigate the morphological changes of an IDR induced by its post-translational modification, as demonstrated by the HS-AFM imaging of FACT [15] and a few others. FACT is a hetero dimer of SPT16 and SSRP1 subunits. The long IDR in SSRP1 contain ten phosphorylation sites residing on the acidic ID segment adjacent to a high-mobility-group (HMG) domain-flanking basic ID segment. The phosphorylation of SSRP1 is known to destabilize the binding of FACT to nucleosomes [43]. To observe structural effects of the phosphorylation of the SSRP1′s IDR, the C-terminal shorter IDR of SPT16 and the *N*-terminal half of SPT16 were deleted. Both phosphorylated and dephosphorylated (the Ser residues on the ten sites were replaced with Ala) forms displayed a similar overall structure; a large globule (GD_1) is connected to the long IDR of SSRP1 (Fig. 6a and b). Moreover, in the two forms, the middle region of the IDR contained a small globule (GD_2) that was appearing and disappearing over time. The small globule contains the HMG of ~ 1 nm size, judging from its position and size (1.1–1.7 nm). Compared to the dephosphorylated form, the small globule and the IDR in the phosphorylated form often took a higher height state and a shorter length state, respectively (Fig. 6c–f). This distinct feature and its physiological relevance can be explained as follows: (i) the acidic segment of SSRP1′s IDR electrostatically interacts with both the region containing the basic segment of SSRP1′s IDR and the HMG to evoke partial folding of the IDR; (ii) the folded and unfolded states are in dynamic equilibrium; (iii) extensive phosphorylation of the IDR's acidic segment shifts the equilibrium toward the folded state; and (iv) this structural bias to the folded state blocks the binding of nucleosomal DNA to the region containing the basic IDR segment and the HMG domain.

5.2. Initial process of membrane less organelle formation

In recent years, MLOs formed through LLPSare one of the hot topics in biology, and IDPs have been recognized as the key players in forming MLOs [3,4]. The formation and dissolution of liquid droplet-like condensates (liquid droplets) are triggered by small changes in the cellular environment (pH, temperature, ionic strength, osmotic pressure, type and concentration of the surrounding biomolecules, and others) and occurs in an avalanche-like manner, like a phase transition phenomenon. Because this property is realized by the multivalent interactions of the molecules constituting liquid droplets, it is perfectly natural that IDPs are involved in the formation of liquid droplets. IDPs are typical molecules that can change their promiscuous, multivalent intra-/intermolecular interactions depending on environment changes and/or their post-translational modifications. HS-AFM can be used to visualize (i) dynamic molecular features of the individual molecules involved in the formation and dissolution of liquid droplets [18,20], (ii) the initial process of droplet formation, and (iii) detailed surface features of the formed droplets.

In yeast, autophagy induced by starvation stress requires the formation of biomolecular complexes called PAS (pre-autophagosomal structure) at the first step [44] but its entity has been elusive. PAS organization initially requires assembly of the Atg1 complex, consisting of Atg1, Atg13, and the Atg17–Atg29–Atg31 complex which forms a characteristic S-shaped backbone due to the dimer shape of Atg17. This supramolecular self-assembly of Atg1 complexes accelerate the initial events of autophagy, including auto phosphorylation of Atg1, recruitment of Atg9 vesicles, and phosphorylation of Atg9 by Atg1. In this event, Atg13, which is dephosphorylated in starvation conditions, plays a key role as a regulatory factor [45].

Atg13 contains regions responsible for binding to Atg17: 17LR (359–389) and 17BR (424–436). The crystal structure of the Atg17-Atg29-Atg31 complex with the $Atg13^{17LR}$ and $Atg13^{17BR}$ peptides shows that two $Atg13^{17BR}$ peptides bind to the distal end of each Atg17

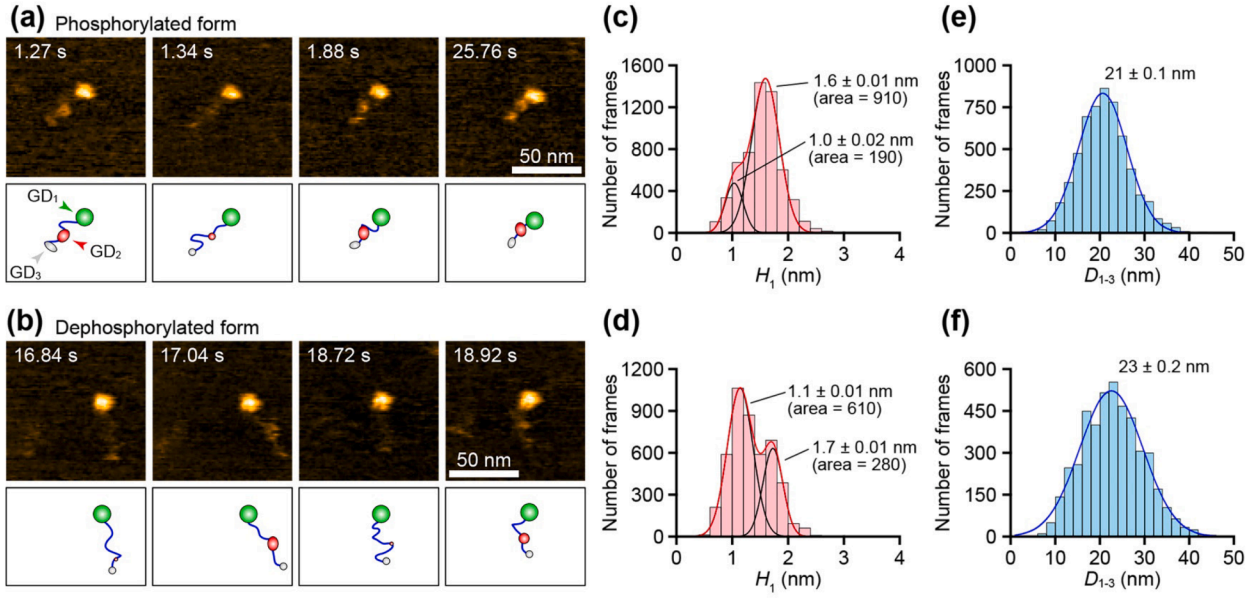

Fig. 6. Phosphorylation-induced morphological changes in FACT. (a, b) Clips of successive HS-AFM images of phosphorylated (a) and dephosphorylated FACT (b). The images were captured with 80 × 80 pixels at ~ 14 fps. Z-scale, 4.0 nm. The observed molecular features are schematized in the bottom panels. In the both constructs, the large globular domain (GD_1, green) is connected to the IDR of SSRP1 on which two small globular domains, termed GD_2 (red) and GD_3 (gray), were found at the middle and at the distal end, respectively. (c, d) Height distributions of GD_2 in phosphorylated (c) and dephosphorylated FACT (d). The histograms appear to have two peaks at 1.6–1.7 and ~ 1.1 nm, which correspond to HMG associated with the IDR and HMG alone, respectively. (e, f) Distributions of the distance between GD_1 and GD_3 in phosphorylated FACT (e) and dephosphorylated FACT (f).

protomer, while two Atg13^{17LR} peptides bind to the dimer interface of Atg17 [18]. The two Atg13 binding sites on an Atg17 protomer is separated approximately by 13 nm. In contrast, the power law mentioned above indicates that the mean R_{2D} value of the constantly disordered region between the 17LR and 17BR is ~ 7.3 nm. This suggests that Atg13 is structurally unable to bind to its two binding sites within the same Atg17 protomer. Therefore, Atg13 binds and cross-links two Atg17 molecules via Atg13^{17LR} and Atg13^{17BR}. This idea was confirmed by the observation that an Atg13 mutant, in which the IDR region between the 17LR and 17BR is deleted, still can induce PAS formation [18]. Furthermore, the HS-AFM observation of the complexes formed by Atg13 and Atg17–Atg29–Atg31 in a solution containing KCl showed an assembled structure in which several S-shaped Atg17 molecules separated by ~ 8 nm were stuck out of a large globular assembly (Fig. 7a), consistent with the above idea. Moreover, a long incubation of a mixture of Atg13 and the Atg17−Atg31 complexes on mica in a solution containing NaCl resulted in the formation of liquid droplets with 100–400 nm in diameter, where globular molecules were observed to be diffusing in and out of the droplets (Fig. 7b) [46]. Note that the S-shape of Atg17 is K^+ ion dependent. Thus, the entity of PAS was revealed to be liquid droplets formed through LLPS.

Next, an example of HS-AFM imaging studies revealing the detailed surface features of liquid droplets is described here. To visualize liquid droplets by HS-AFM, the HS-AFM setup combined with a fluorescent microscope is useful [47,48]. This is because the maximum scanning area of HS-AFM is usually a few square micrometers, while liquid droplets are usually formed sparsely over a wider area. Therefore, the fluorescence imaging of liquid droplets helps bring the AFM tip to their locations. The liquid droplets formed from a mixture of Atg13 and the Atg17–Atg29–Atg31 complexes in a solution containing KCl were observed by HS-AFM, in which Atg13 and Atg17 were labeled with different fluorescent dyes [25]. When the droplets were gently placed onto a cleaned coverslip, molecules with an S-shape, a distinctive feature of Atg17 [49], were distributed irregularly throughout these droplets (Fig. 7c). Importantly, S-shaped Atg17 molecules exhibited nanoscopic diffusional motion within the droplets, providing further evidence that the droplets are in a liquid-like state. By contrast, when the droplets were placed onto a positively charged coverslip, Atg17 was regularly arranged in the droplets and showed little movement in droplets (Fig. 7d). This observation suggests that the droplets can mature to a static, solid-like structure depending on the environment, consistent with the other biomolecular condensates that transit from liquid droplets to solid-like states such as gels, glasses and amyloids [50]. These results demonstrate the advantage of HS-AFM that can observe the dynamic nanoscopic features of biomolecules on the droplet surface, although HS-AFM cannot observe the interior of the droplets.

The phase-separated droplets with liquid-like properties are often made through weak intermolecular interactions with dissociation constants in the range of a few μM or larger. To visualize them without mechanical disturbance by the AFM tip, it is sometimes necessary to slightly cross-link the constituting biomolecules with glutaraldehyde [25,51]. Although this mechanical disturbance is a weak point of AFM measurements, this feature may be used to determine which molecules are weakly interacting in a droplet. HS-AFM observations of various types of phase-separated droplets will provide further insights into their assembly mechanism and mechanical properties.

5.3. Cross-β polymerization of low complexity regions

Many IDRs have unusual regions made up of only a few different types of amino acids and its repeats called low complexity domains (LCDs) [52,53]. LCDs seen in IDRs are often found in the activation domains of many transcription factors [54] and RNA-binding proteins involved in stress response and neurodegenerative diseases such as amyotrophic lateral sclerosis [55–58]. Notably, in recent years, IDPs with LCDs (e.g, FUS, hnRNPA1, hnRNPA2, TIA-1, TDP-43, ataxin-2, Sup35, etc.) have been observed to form phase-separated droplets in which cross-β fibers are formed [59–63]. Here, the recent HS-AFM observations of the fibrillation process of Sup35 are described [22].

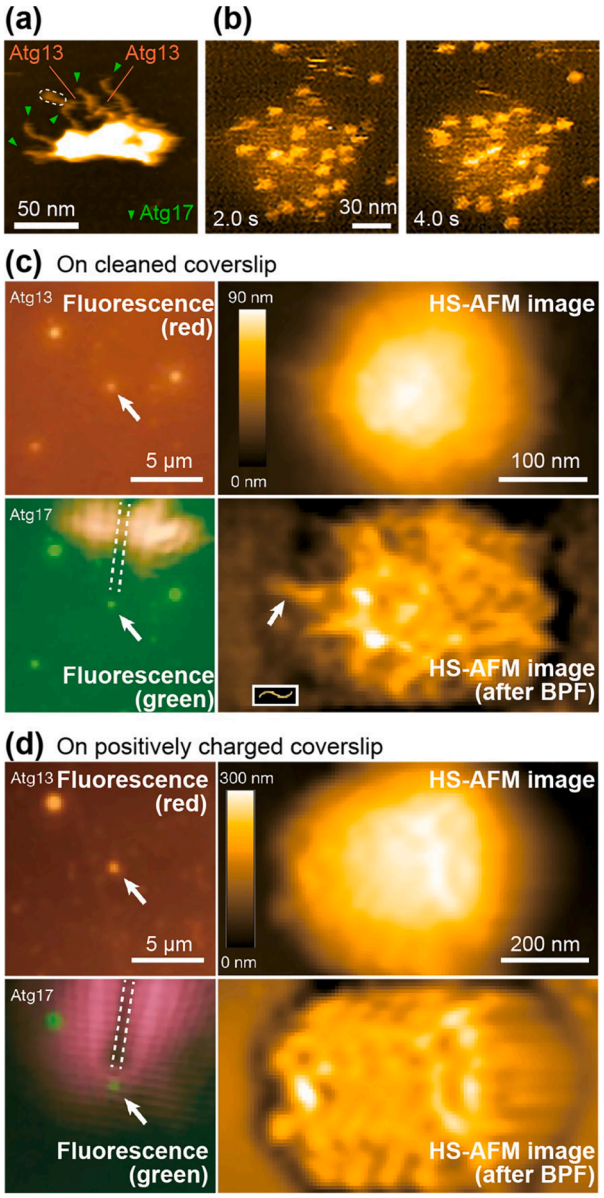

Fig. 7. HS-AFM images showing membrane-less organelle related to autophagy. (a) Complexes formed by mixing of dephosphorylated Atg13 and Atg17 in a solution containing KCl. The green arrowheads point to S-shaped Atg17 molecules extending from the protein aggregate. The particle encircled with the broken line is an unconfirmed object. (b) Liquid droplet formed after a long incubation of dephosphorylated Atg13 and the Atg17Atg31 complexes on mica, in a solution containing NaCl. (c, d) Liquid droplet-like condensate observed on a cleaned coverslip (c) and solid-like condensate on a positively charged coverslip (d), which are formed in a 1:1 mixture of Atg13–SNAP (labeled with Surface 549, red fluorophore) and SNAP–Atg17 (labeled with Alexa Fluor 488, green fluorophore), in a solution containing KCl. The left and right images are those of florescence and HS-AFM, respectively. The dotted lines (left bottom) indicate an AFM cantilever. The HS-AFM image (right bottom) is obtained by band-pass filtering of the right top image. The inset in the right bottom image of (c) shows the dimeric Atg17 structure in the same scale.

Sup35, an IDP working as a translation termination factor in yeast, is known as a prion protein that forms amyloid fibrils [64]. Sup35 have recently been shown to form phase-separated droplets depending on the nutritional status of yeast in which the translational activity is impaired

[59]. For the HS-AFM observations, the NM domain involved in amyloid formation of Sup35 (Sup35NM) was used [22]. The monomer form of Sup35NM exhibited two highly flexible tail-like structures sticking out of a small globular domain, consistent with previous reports [65–67]. Sup35NM formed spherical oligomers with a height of about 4 nm during incubation for 60 min. However, no amyloid fibrils were formed from these oligomers even after several hours of incubation. Amyloid fibrils appeared after much longer incubation (for more than 2 days). Fibril elongation was not seen by addition of the oligomers to fibril seeds but occurred unidirectionally by monomer addition (Fig. 8a), as previously reported [68,69]. The growing fibrils were fragile and occasionally fragmented during HS-AFM imaging, providing new seeds for fibril elongation (Fig. 8b). Notably, the fibril elongation occurred smoothly without discrete steps even in high-resolution imaging, suggesting gradual conversion of the incorporated monomers into cross-β structures. Maybe more intriguingly, HS-AFM images showed that the oligomers were interspaced with a similar size of gaps (Fig. 8c), suggesting that they are mutually repulsive. Interspace gaps were also observed between a fibril and the oligomers surrounding it (Fig. 8c). The gap size between adjacent oligomers was distributed around ~ 6 nm, while the gap size between a fibril and its neighboring oligomers was distributed around ~ 10 nm. Because these gap sizes were much larger than the Debye Hückel distance of the ionic solution (0.72 nm) and independent of ionic strength, the gaps were likely to have originated from the flexible regions of Sup35NM extending out from the oligomers and fibrils. In fact, tail-like structures were confirmed to extend from oligomers by faster imaging at 17 fps (Fig. 8d). Tail-like structures were also observed to extend from the lateral side of fibrils but their motion could be detected even with imaging at 1 fps, indicating they are relatively solid and not freely moving (Fig. 8e). These extending structures seem to repel oligomers from the lateral side of the fibrils, which may play a role in the growth of straight fibrils without branching. Notably, such structures were not observed at the fibril ends (Fig. 8e), and therefore, oligomers could approach to the fibril ends, although their incorporation into the fibril ends were never observed. The mutual repelling effect of IDRs found in this study may be commonly possessed by other IDPs and possibly involved in their functions.

6. Outlook

HS-AFM is a relatively new microscopy technique but its system products and small cantilevers essentially required for HS-AFM are

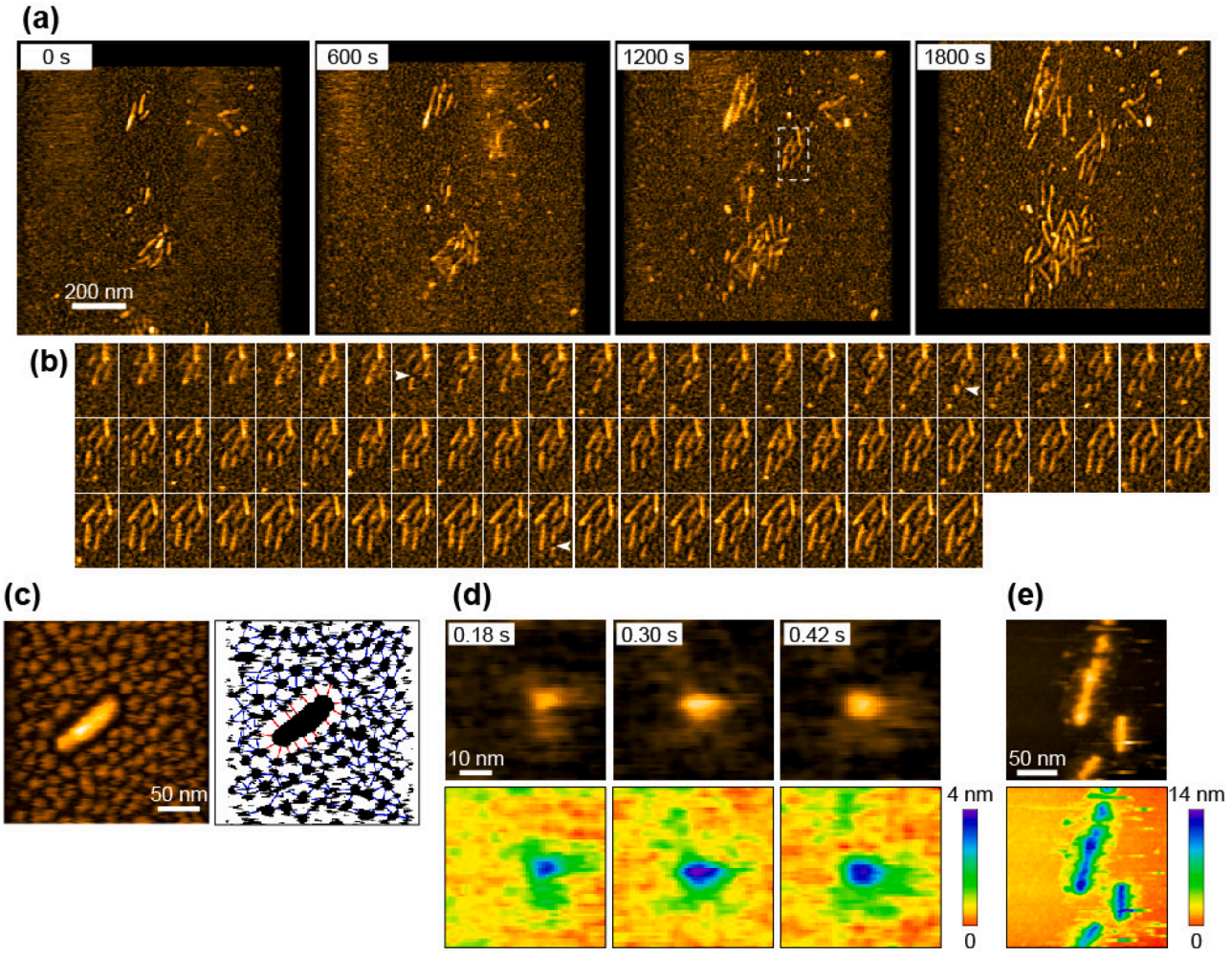

Fig. 8. HS-AFM images showing amyloid fibril formation by Sup35NM. (a) Representative HS-AFM images of growing Sup35NM fibrils captured after 50-min preincubation on mica. The images were captured with 400 × 400 pixels at 0.1 fps. Z-scale, 10 nm. (b) Successive HS-AFM images showing seed-dependent fibril growth and fragmentation. The images are those clipped from the region highlighted by dashed line in (a, 1200 s). The fragmented positions are indicated by arrowheads. (c) HS-AFM image of a fibril surrounded with oligomers with height of ~ 4 nm, and its sketch with lines representing inter-particle gaps. (d) HS-AFM images showing Sup35NM oligomers. The images were captured with 80 × 80 pixels at 16.7 fps. Z-scale, 4 nm. (e) HS-AFM image showing Sup35NM fibrils with some structures extending from the lateral side. The image was captured with 200 × 200 pixels at 1 fps. Z-scale, 14 nm. The bottom images of (d, e) are height display in rainbow color of the corresponding upper images.

already commercially available. Experimental protocols to visualize the dynamic structure and processes of biomolecules have been gradually established [36,70–72] along with continuously increasing imaging studies with HS-AFM [13,73,74]. The greatest advantage of HS-AFM visualization is that it allows us to simultaneously find several (often unexpected) facts of the biolomolecules under the microscope. The visualized images can be understood without complicated and round-about interpretations. Of course, quantitative image analyses are often required be done for produced many images. Nevertheless, HS-AFM has so far been used mostly for structured proteins, whereas the number of HS-AFM studies on IDPs is limited. It is expected that this microcopy will be applied to a much wider range of IDPs and related biological phenomena in the near future, which will bring a vast array of new discoveries that are impossible with other techniques. Many IDPs are involved in gene regulation and often associated with diseases. For example, MeCP2 is involved in neurodevelopmental diseases [75,76], and the fusion proteins such as EML4-ALK [77] and SS18-SSX [78,79] cause lung cancer and synovial sarcoma, respectively. Thus, new information about their dynamic structures and processes to be revealed by HS-AFM surely provide clues to understanding and solving diseases. On the other hand, as shown in the observations of MLOs, the current HS-AFM sometimes disrupt weak bimolecular interactions. However, efforts to solve this inconvenience have been continued. New techniques recently developed in our group have already enhanced the non-disturbing and speed performances of HS-AFM [37–39]. Thus, we expect that HS-AFM will be applied to a much wider range of biomolecular systems involving very weak molecular interactions and faster processes.

Declaration of Competing Interest

The authors declare that they have no known competing financial interests or personal relationships that could have appeared to influence the work reported in this paper.

Acknowledgements

The authors would like to thank Steven McArthur for helpful suggestions resulting in the improvement of this work. This work was supported by the CREST program of JST (#JPMJCR13M1 to TA, #JPMJCR1762 to NK), KAKENHI of JSPS (#26119003 and #17H06121 to TA, and #20H00327 to NK) and World Premier International Research Center Initiative (WPI) of the Ministry of Education, Culture, Sports, Science and Technology (MEXT), Japan.

References

[1] V.N. Uversky, J.R. Gillespie, A.L. Fink, Why are “natively unfolded” proteins unstructured under physiologic conditions? Proteins 41 (3) (2000) 415–427.
[2] P.E. Wright, H.J. Dyson, Intrinsically disordered proteins in cellular signalling and regulation, Nature reviews, Mol. Cell Biol. 16 (1) (2015) 18–29.
[3] S.F. Banani, H.O. Lee, A.A. Hyman, M.K. Rosen, Biomolecular condensates: organizers of cellular biochemistry, Nat. Rev. Mol. Cell Biol. 18 (5) (2017) 285–298.
[4] V.N. Uversky, Intrinsically disordered proteins in overcrowded milieu: Membrane-less organelles, phase separation, and intrinsic disorder, Curr. Opin. Struct. Biol. 44 (2017) 18–30.
[5] J. Habchi, P. Tompa, S. Longhi, V.N. Uversky, Introducing protein intrinsic disorder, Chem. Rev. 114 (13) (2014) 6561–6588.
[6] P. Bernado, E. Mylonas, M.V. Petoukhov, M. Blackledge, D.I. Svergun, Structural characterization of flexible proteins using small-angle X-ray scattering, J. Am. Chem. Soc. 129 (17) (2007) 5656–5664.
[7] C. Camilloni, A. De Simone, W.F. Vranken, M. Vendruscolo, Determination of secondary structure populations in disordered states of proteins using nuclear magnetic resonance chemical shifts, Biochemistry 51 (11) (2012) 2224–2231.
[8] G. Tria, H.D. Mertens, M. Kachala, D.I. Svergun, Advanced ensemble modelling of flexible macromolecules using X-ray solution scattering, IUCrJ 2 (Pt 2) (2015) 207–217.
[9] B. Schuler, A. Soranno, H. Hofmann, D. Nettels, Single-Molecule FRET Spectroscopy and the Polymer Physics of Unfolded and Intrinsically Disordered Proteins, Annu. Rev. Biophys. 45 (2016) 207–231.
[10] U.R. Shrestha, P. Juneja, Q. Zhang, V. Gurumoorthy, J.M. Borreguero, V. Urban, X. Cheng, S.V. Pingali, J.C. Smith, H.M. O’Neill, L. Petridis, Generation of the configurational ensemble of an intrinsically disordered protein from unbiased molecular dynamics simulation, PNAS 116 (41) (2019) 20446–20452.
[11] W. Wang, Recent advances in atomic molecular dynamics simulation of intrinsically disordered proteins, Phys. Chem. Chem. Phys. 23 (2) (2021) 777–784.
[12] T. Ando, N. Kodera, E. Takai, D. Maruyama, K. Saito, A. Toda, A high-speed atomic force microscope for studying biological macromolecules, PNAS 98 (22) (2001) 12468–12472.
[13] T. Ando, T. Uchihashi, S. Scheuring, Filming biomolecular processes by high-speed atomic force microscopy, Chem. Rev. 114 (6) (2014) 3120–3188.
[14] A. Miyagi, Y. Tsunaka, T. Uchihashi, K. Mayanagi, S. Hirose, K. Morikawa, T. Ando, Visualization of intrinsically disordered regions of proteins by high-speed atomic force microscopy, Chemphyschem 9 (13) (2008) 1859–1866.
[15] M. Hashimoto, N. Kodera, Y. Tsunaka, M. Oda, M. Tanimoto, T. Ando, K. Morikawa, S. Tate, Phosphorylation-coupled intramolecular dynamics of unstructured regions in chromatin remodeler FACT, Biophys. J. 104 (10) (2013) 2222–2234.
[16] S. Ishino, T. Yamagami, M. Kitamura, N. Kodera, T. Mori, S. Sugiyama, T. Ando, N. Goda, T. Tenno, H. Hiroaki, Y. Ishino, Multiple interactions of the intrinsically disordered region between the helicase and nuclease domains of the archaeal Hef protein, J. Biol. Chem. 289 (31) (2014) 21627–21639.
[17] N. Kodera, K. Uchida, T. Ando, S. Aizawa, Two-ball structure of the flagellar hook-length control protein FliK as revealed by high-speed atomic force microscopy, J. Mol. Biol. 427 (2) (2015) 406–414.
[18] H. Yamamoto, Y. Fujioka, S.W. Suzuki, D. Noshiro, H. Suzuki, C. Kondo-Kakuta, Y. Kimura, H. Hirano, T. Ando, N.N. Noda, Y. Ohsumi, The Intrinsically Disordered Protein Atg13 Mediates Supramolecular Assembly of Autophagy Initiation Complexes, Dev. Cell 38 (1) (2016) 86–99.
[19] N. Kodera, D. Noshiro, S.K. Dora, T. Mori, J. Habchi, D. Blocquel, A. Gruet, M. Dosnon, E. Salladini, C. Bignon, Y. Fujioka, T. Oda, N.N. Noda, M. Sato, M. Lotti, M. Mizuguchi, S. Longhi, T. Ando, Structural and dynamics analysis of intrinsically disordered proteins by high-speed atomic force microscopy, Nat. Nanotechnol. 16 (2) (2021) 181–189.
[20] A. Sakane, T.A. Yano, T. Uchihashi, K. Horikawa, Y. Hara, I. Imoto, S. Kurisu, H. Yamada, K. Takei, T. Sasaki, JRAB/MICAL-L2 undergoes liquid-liquid phase separation to form tubular recycling endosomes, Commun. Biol. 4 (1) (2021) 551.
[21] N. Terahara, N. Kodera, T. Uchihashi, T. Ando, K. Namba, T. Minamino, Na(+)-induced structural transition of MotPS for stator assembly of the Bacillus flagellar motor, Sci. Adv. 3 (11) (2017) eaao4119.
[22] H. Konno, T. Watanabe-Nakayama, T. Uchihashi, M. Okuda, L. Zhu, N. Kodera, Y. Kikuchi, T. Ando, H. Taguchi, Dynamics of oligomer and amyloid fibril formation by yeast prion Sup35 observed by high-speed atomic force microscopy, PNAS 117 (14) (2020) 7831–7836.
[23] T. Watanabe-Nakayama, M. Nawa, H. Konno, N. Kodera, T. Ando, D.B. Teplow, K. Ono, Self- and Cross-Seeding on alpha-Synuclein Fibril Growth Kinetics and Structure Observed by High-Speed Atomic Force Microscopy, ACS Nano 14 (8) (2020) 9979–9989.
[24] H. Imai, T. Uchiumi, N. Kodera, Direct visualization of translational GTPase factor pool formed around the archaeal ribosomal P-stalk by high-speed AFM, PNAS 117 (51) (2020) 32386–32394.
[25] Y. Fujioka, J.M. Alam, D. Noshiro, K. Mouri, T. Ando, Y. Okada, A.I. May, R. L. Knorr, K. Suzuki, Y. Ohsumi, N.N. Noda, Phase separation organizes the site of autophagosome formation, Nature 578 (7794) (2020) 301–305.
[26] Q. Zhong, D. Inniss, K. Kjoller, V.B. Elings, Fractured Polymer Silica Fiber Surface Studied by Tapping Mode Atomic-Force Microscopy, Surf. Sci. 290 (1–2) (1993) L688–L692.
[27] P.K. Hansma, J.P. Cleveland, M. Radmacher, D.A. Walters, P.E. Hillner, M. Bezanilla, M. Fritz, D. Vie, H.G. Hansma, C.B. Prater, J. Massie, L. Fukunaga, J. Gurley, V. Elings, Tapping Mode Atomic-Force Microscopy in Liquids, Appl. Phys. Lett. 64 (13) (1994) 1738–1740.
[28] C.A.J. Putman, K.O. Vanderwerf, B.G. Degrooth, N.F. Vanhulst, J. Greve, Tapping Mode Atomic-Force Microscopy in Liquid, Appl. Phys. Lett. 64 (18) (1994) 2454–2456.
[29] N. Kodera, M. Sakashita, T. Ando, Dynamic proportional-integral-differential controller for high-speed atomic force microscopy, Rev. Sci. Instrum. 77 (8) (2006).
[30] N. Kodera, H. Yamashita, T. Ando, Active damping of the scanner for high-speed atomic force microscopy, Rev. Sci. Instrum. 76 (5) (2005).
[31] T. Ando, T. Uchihashi, T. Fukuma, High-speed atomic force microscopy for nano-visualization of dynamic biomolecular processes, Prog. Surf. Sci. 83 (7–9) (2008) 337–437.
[32] T. Ando, High-speed Atomic Force Microscopy in Biology, Springer-Verlag GmbH Germany, 2022, p. 319.
[33] T. Ando, Molecular machines directly observed by high-speed atomic force microscopy, FEBS Lett. 587 (8) (2013) 997–1007.
[34] T. Uchihashi, R. Iino, T. Ando, H. Noji, High-speed atomic force microscopy reveals rotary catalysis of rotorless F(1)-ATPase, Science 333 (6043) (2011) 755–758.
[35] N. Kodera, H. Abe, P.D.N. Nguyen, S. Ono, Native cyclase-associated protein and actin from Xenopus laevis oocytes form a unique 4:4 complex with a tripartite structure, J. Biol. Chem. 296 (2021), 100649.
[36] T. Uchihashi, N. Kodera, T. Ando, Guide to video recording of structure dynamics and dynamic processes of proteins by high-speed atomic force microscopy, Nat. Protoc. 7 (6) (2012) 1193–1206.
[37] S. Fukuda, T. Ando, Faster high-speed atomic force microscopy for imaging of biomolecular processes, Rev. Sci. Instrum. 92 (3) (2021), 033705.

[38] K. Umeda, C. Okamoto, M. Shimizu, S. Watanabe, T. Ando, N. Kodera, Architecture of zero-latency ultrafast amplitude detector for high-speed atomic force microscopy, Appl. Phys. Lett. 119 (18) (2021), 181602.
[39] M. Shimizu, C. Okamoto, K. Umeda, S. Watanabe, T. Ando, N. Kodera, An ultrafast piezoelectric Z-scanner with a resonance frequency above 1.1 MHz for high-speed atomic force microscopy, Rev. Sci. Instrum. 93 (1) (2022), 013701.
[40] K.X. Ngo, N. Kodera, E. Katayama, T. Ando, T.Q. Uyeda, Cofilin-induced unidirectional cooperative conformational changes in actin filaments revealed by high-speed atomic force microscopy, eLife 4 (2015), e04806.
[41] S. Milles, M.R. Jensen, C. Lazert, S. Guseva, S. Ivashchenko, G. Communie, D. Maurin, D. Gerlier, R.W.H. Ruigrok, M. Blackledge, An ultraweak interaction in the intrinsically disordered replication machinery is essential for measles virus function, Sci. Adv. 4 (8) (2018) eaat7778.
[42] J. Habchi, L. Mamelli, H. Darbon, S. Longhi, Structural disorder within Henipavirus nucleoprotein and phosphoprotein: from predictions to experimental assessment, PLoS ONE 5 (7) (2010), e11684.
[43] Y. Tsunaka, J. Toga, H. Yamaguchi, S. Tate, S. Hirose, K. Morikawa, Phosphorylated intrinsically disordered region of FACT masks its nucleosomal DNA binding elements, J. Biol. Chem. 284 (36) (2009) 24610–24621.
[44] K. Suzuki, T. Kirisako, Y. Kamada, N. Mizushima, T. Noda, Y. Ohsumi, The pre-autophagosomal structure organized by concerted functions of APG genes is essential for autophagosome formation, EMBO J. 20 (21) (2001) 5971–5981.
[45] Y. Fujioka, S.W. Suzuki, H. Yamamoto, C. Kondo-Kakuta, Y. Kimura, H. Hirano, R. Akada, F. Inagaki, Y. Ohsumi, N.N. Noda, Structural basis of starvation-induced assembly of the autophagy initiation complex, Nat. Struct. Mol. Biol. 21 (6) (2014) 513–521.
[46] N. Kodera, T. Ando, Visualization of intrinsically disordered proteins by high-speed atomic force microscopy, Curr. Opin. Struct. Biol. 72 (2022) 260–266.
[47] S. Fukuda, T. Uchihashi, R. Iino, Y. Okazaki, M. Yoshida, K. Igarashi, T. Ando, High-speed atomic force microscope combined with single-molecule fluorescence microscope, Rev. Sci. Instrum. 84 (7) (2013), 073706.
[48] M. Shibata, T. Uchihashi, T. Ando, R. Yasuda, Long-tip high-speed atomic force microscopy for nanometer-scale imaging in live cells, Sci. Rep. 5 (2015) 8724.
[49] M.J. Ragusa, R.E. Stanley, J.H. Hurley, Architecture of the Atg17 complex as a scaffold for autophagosome biogenesis, Cell 151 (7) (2012) 1501–1512.
[50] J.B. Woodruff, A.A. Hyman, E. Boke, Organization and function of non-dynamic biomolecular condensates, Trends Biochem. Sci. 43 (2) (2018) 81–94.
[51] A. Yamasaki, J.M. Alam, D. Noshiro, E. Hirata, Y. Fujioka, K. Suzuki, Y. Ohsumi, N. N. Noda, Liquidity Is a critical determinant for selective autophagy of protein condensates, Mol. Cell 77 (6) (2020) 1163–1175.e9.
[52] C.J. Oldfield, A.K. Dunker, Intrinsically disordered proteins and intrinsically disordered protein regions, Annu. Rev. Biochem. 83 (2014) 553–584.
[53] S.M. Cascarina, M.R. Elder, E.D. Ross, Atypical structural tendencies among low-complexity domains in the Protein Data Bank proteome, PLoS Comput. Biol. 16 (1) (2020), e1007487.
[54] P.B. Sigler, Transcriptional activation. Acid blobs and negative noodles, Nature 333 (6170) (1988) 210–212.
[55] M. Kato, T.W. Han, S. Xie, K. Shi, X. Du, L.C. Wu, H. Mirzaei, E.J. Goldsmith, J. Longgood, J. Pei, N.V. Grishin, D.E. Frantz, J.W. Schneider, S. Chen, L. Li, M. R. Sawaya, D. Eisenberg, R. Tycko, S.L. McKnight, Cell-free formation of RNA granules: low complexity sequence domains form dynamic fibers within hydrogels, Cell 149 (4) (2012) 753–767.
[56] O.D. King, A.D. Gitler, J. Shorter, The tip of the iceberg: RNA-binding proteins with prion-like domains in neurodegenerative disease, Brain Res. 1462 (2012) 61–80.
[57] S. Calabretta, S. Richard, Emerging Roles of Disordered Sequences in RNA-Binding Proteins, Trends Biochem. Sci. 40 (11) (2015) 662–672.
[58] J.P. Taylor, R.H. Brown Jr., D.W. Cleveland, Decoding ALS: from genes to mechanism, Nature 539 (7628) (2016) 197–206.
[59] T.M. Franzmann, M. Jahnel, A. Pozniakovsky, J. Mahamid, A.S. Holehouse, E. Nuske, D. Richter, W. Baumeister, S.W. Grill, R.V. Pappu, A.A. Hyman, S. Alberti, Phase separation of a yeast prion protein promotes cellular fitness, Science 359 (6371) (2018) eaao5654.
[60] M. Kato, Y.S. Yang, B.M. Sutter, Y. Wang, S.L. McKnight, B.P. Tu, Redox state controls phase separation of the yeast ataxin-2 protein via reversible oxidation of its methionine-rich low-complexity domain, Cell 177 (3) (2019) 711–721.e8.
[61] Y.S. Yang, M. Kato, X. Wu, A. Litsios, B.M. Sutter, Y. Wang, C.H. Hsu, N.E. Wood, A. Lemoff, H. Mirzaei, M. Heinemann, B.P. Tu, Yeast ataxin-2 forms an intracellular condensate required for the inhibition of TORC1 signaling during respiratory growth, Cell 177 (3) (2019) 697–710.e17.
[62] X. Gui, F. Luo, Y. Li, H. Zhou, Z. Qin, Z. Liu, J. Gu, M. Xie, K. Zhao, B. Dai, W. S. Shin, J. He, L. He, L. Jiang, M. Zhao, B. Sun, X. Li, C. Liu, D. Li, Structural basis for reversible amyloids of hnRNPA1 elucidates their role in stress granule assembly, Nat. Commun. 10 (1) (2019) 2006.
[63] X.F. Zhuo, J. Wang, J. Zhang, L.L. Jiang, H.Y. Hu, J.X. Lu, Solid-State NMR Reveals the Structural Transformation of the TDP-43 Amyloidogenic Region upon Fibrillation, J. Am. Chem. Soc. 142 (7) (2020) 3412–3421.
[64] G. Zhouravleva, L. Frolova, X. Le Goff, R. Le Guellec, S. Inge-Vechtomov, L. Kisselev, M. Philippe, Termination of translation in eukaryotes is governed by two interacting polypeptide chain release factors, eRF1 and eRF3, EMBO J. 14 (16) (1995) 4065–4072.
[65] C.Y. King, P. Tittmann, H. Gross, R. Gebert, M. Aebi, K. Wuthrich, Prion-inducing domain 2–114 of yeast Sup35 protein transforms in vitro into amyloid-like filaments, PNAS 94 (13) (1997) 6618–6622.
[66] J.R. Glover, A.S. Kowal, E.C. Schirmer, M.M. Patino, J.J. Liu, S. Lindquist, Self-seeded fibers formed by Sup35, the protein determinant of [PSI+], a heritable prion-like factor of S. cerevisiae, Cell 89 (5) (1997) 811–819.
[67] S. Mukhopadhyay, R. Krishnan, E.A. Lemke, S. Lindquist, A.A. Deniz, A natively unfolded yeast prion monomer adopts an ensemble of collapsed and rapidly fluctuating structures, PNAS 104 (8) (2007) 2649–2654.
[68] Y. Inoue, A. Kishimoto, J. Hirao, M. Yoshida, H. Taguchi, Strong growth polarity of yeast prion fiber revealed by single fiber imaging, J. Biol. Chem. 276 (38) (2001) 35227–35230.
[69] S.R. Collins, A. Douglass, R.D. Vale, J.S. Weissman, Mechanism of prion propagation: amyloid growth occurs by monomer addition, PLoS Biol. 2 (10) (2004), e321.
[70] D. Yamamoto, T. Uchihashi, N. Kodera, H. Yamashita, S. Nishikori, T. Ogura, M. Shibata, T. Ando, High-speed atomic force microscopy techniques for observing dynamic biomolecular processes, Methods Enzymol. 475 (2010) 541–564.
[71] Y.L. Lyubchenko, L.S. Shlyakhtenko, T. Ando, Imaging of nucleic acids with atomic force microscopy, Methods 54 (2) (2011) 274–283.
[72] S. Banerjee, Y.L. Lyubchenko, Topographically smooth and stable supported lipid bilayer for high-resolution AFM studies, Methods 197 (2022) 13–19.
[73] T. Ando, High-speed atomic force microscopy, Curr. Opin. Chem. Biol. 51 (2019) 105–112.
[74] G.R. Heath, S. Scheuring, Advances in high-speed atomic force microscopy (HS-AFM) reveal dynamics of transmembrane channels and transporters, Curr. Opin. Struct. Biol. 57 (2019) 93–102.
[75] R.R. Meehan, J.D. Lewis, S. McKay, E.L. Kleiner, A.P. Bird, Identification of a mammalian protein that binds specifically to DNA containing methylated CpGs, Cell 58 (3) (1989) 499–507.
[76] M. Chahrour, H.Y. Zoghbi, The story of Rett syndrome: from clinic to neurobiology, Neuron 56 (3) (2007) 422–437.
[77] M. Soda, Y.L. Choi, M. Enomoto, S. Takada, Y. Yamashita, S. Ishikawa, S. Fujiwara, H. Watanabe, K. Kurashina, H. Hatanaka, M. Bando, S. Ohno, Y. Ishikawa, H. Aburatani, T. Niki, Y. Sohara, Y. Sugiyama, H. Mano, Identification of the transforming EML4-ALK fusion gene in non-small-cell lung cancer, Nature 448 (7153) (2007) 561–566.
[78] N.R. dos Santos, D.R. de Bruijn, A.G. van Kessel, Molecular mechanisms underlying human synovial sarcoma development, Genes Chromosom. Cancer 30 (1) (2001) 1–14.
[79] M. Ladanyi, C.R. Antonescu, D.H. Leung, J.M. Woodruff, A. Kawai, J.H. Healey, M. F. Brennan, J.A. Bridge, J.R. Neff, F.G. Barr, J.D. Goldsmith, J.S. Brooks, J. R. Goldblum, S.Z. Ali, J. Shipley, C.S. Cooper, C. Fisher, B. Skytting, O. Larsson, Impact of SYT-SSX fusion type on the clinical behavior of synovial sarcoma: a multi-institutional retrospective study of 243 patients, Cancer Res. 62 (1) (2002) 135–140.